Suplemento de la Revista Mexicana de Física **1** (2) 1–7 JUNE–JULY 2020

Flow around a Wingmill device for energy extraction

D. F. Balam-Tamayo and B. Figueroa-Espinoza
Universidad Nacional Autónoma de México, Instituto de Ingeniería.

C. Málaga
Universidad Nacional Autónoma de México, Facultad de Ciencias.
e-mail: cmi.ciencias@ciencias.unam.mx

Received 10 December 2019; accepted 5 March 2020

The dynamics of a closed loop self controlled underwater oscillating foil device for energy extraction (a wingmill) is studied through numerical simulations. The viscous two and three dimensional flow around the foil was computed using OpenFOAM and a Lattice-Boltzmann Equation model, respectively. Heaving is driven by the computed hydrodynamic lift and a damper, that extracts energy, while pitching is driven by the hydrodynamic torque and a feedback control torque that leads the foil to a given angle of attack. Unlike most of the related work found in the literature, the heaving and pitching motion of the foil is not prescribed. Dimensional analysis suggests a compromise between the generator and control gain, and so a parametric study was carried out. The effect of the three dimensional finite wingspan on the performance of the device and the flow is compared with the two dimensional case. This fully coupled fluid-solid-body interaction configuration will allow for the system identification, control and optimization of energy harvesting devices in future studies.

Keywords: Wingmill; hydrofoil; tidal energy

1. Introduction

The idea of using oscillating foils immersed in a stream (called wingmills) for the purpose of harvesting energy dates arguably from the nineteen seventies [1]. The device on the seminal work of Mckinney and DeLaurier [1] consisted of a wing of uniform profile that could rotate to adjust the angle of attack and produce an oscillating heaving motion driven by the lift exerted by the flow. The energy was extracted from the heaving motion. Although the reported efficiency was comparable to that of conventional turbines, the device remained in the shadows until not so long ago [2].

Wingmills present some advantages with respect to conventional rotating configurations. The motion of the foil is more uniform and slower than those on turbines, so marine life would have less probability of harm when swimming close to the device [3, 4]. Wingmill foils are also subject to weaker and more uniform stresses in comparison with those in turbines that are also twisted by the flow. Additionally, wingmills can operate in shallow near-shore waters and are an appealing option for small-scale devices to extract energy from tidal currents for coastal communities [5].

Some prototypes have being developed motivated by the high efficiency possibilities and other potential advantages [6, 7]. Several numerical and experimental investigations can be found in the literature, many of them were reviewed by Young *et al.* [2] and Xiao and Zhu [8]. To the best of our knowledge, there are no reported implementations of feedback control of oscillating foils, where the fluid-solid-body interaction is taken into account for energy harvesting purposes. On the other hand, the three dimensional case has received little attention and shows a lower efficiency than that predicted by two dimensional devices [9]. On the contrary, ground effects and shear flows tend to increase efficiency [10, 11]. In any case, both three dimensional and ground effects have been studied imposing the foil kinematics. The problem is that it has been observed that restrictions in the motion of pitching foils can produce hydrodynamic forces an order of magnitude larger than those observed once restrictions are removed [12] and this can lead to over estimations of the performance.

Here we study the performance of a two dimensional as well as a finite wingspan (three dimensional) wingmill, with no imposed kinematics. The foil motion is driven by hydrodynamic forces and torques, a damper extracting energy from its vertical motion, and a feedback actuator following a simple control law that applies a torque in order to set an angle of attack to increase lift and flip the foil to produce an oscillatory heaving motion.

2. Problem statement

The system consists of a NACA0015 airfoil of span s and chord c immersed in a uniform flow with viscosity μ and density ρ and upstream velocity $\boldsymbol{U}$. For simplicity, the foil mass density is taken to be that of the fluid surrounding it. The foil can move vertically and rotate around its center of mass, placed at $0.25c$ from the leading edge, which corresponds to the center of mass of the foil of uniform density. Figure 1 shows a cross sectional diagram of the system, where the generator (the damper) is included.

In order to compute the hydrodynamic forces on the foil, Navier-Stokes equations for an incompressible flow have to be solved, these are

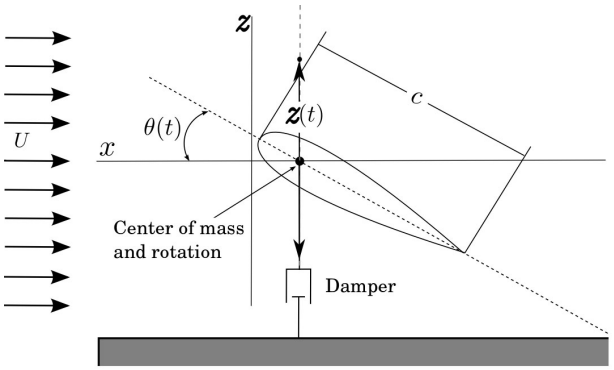

FIGURE 1. Diagram of the cross sectional view of the wingmill system.

$$\nabla \cdot \boldsymbol{u} = 0, \tag{1}$$

$$\rho \frac{D\boldsymbol{u}}{Dt} = -\nabla p + \mu \nabla^2 \boldsymbol{u}, \tag{2}$$

where $\boldsymbol{u}(\boldsymbol{x}, t)$ and $p(\boldsymbol{x}, t)$ are the fluid velocity and pressure fields in the Eulerian description, respectively, and $D/Dt = \partial/\partial t + \boldsymbol{u} \cdot \nabla$ is the lagrangian time derivative. No-slip boundary conditions on $\boldsymbol{u}$ must be imposed on the foil surface, and a uniform flow $\boldsymbol{u} = U\hat{\boldsymbol{e}}_x$ is set far upstream. The hydrodynamic vertical force F_z (the lift on the foil) and horizontal torque T_y are computed through surface integrals of the fluid stress tensor $\boldsymbol{\sigma}(\boldsymbol{x}, t) = -p\mathcal{I} + (1/2)\mu(\nabla \boldsymbol{u} + \nabla \boldsymbol{u}^T)$,

$$F_z(t) = \hat{\boldsymbol{e}}_z \cdot \int_{\mathcal{S}} \boldsymbol{\sigma} \cdot \hat{\boldsymbol{n}} ds, \tag{3}$$

$$T_y(t) = \hat{\boldsymbol{e}}_y \cdot \int_{\mathcal{S}} (\boldsymbol{x} - \boldsymbol{X}) \times (\boldsymbol{\sigma} \cdot \hat{\boldsymbol{n}}) ds, \tag{4}$$

where $\boldsymbol{X}$ is the position of the center of mass, $\hat{\boldsymbol{e}}_z$ and $\hat{\boldsymbol{e}}_y$ are unit vectors in the z and y directions, respectively. $\mathcal{S}$ represents the foil surface, $\hat{\boldsymbol{n}}$ the unit vector normal to $\mathcal{S}$ pointing to the fluid and $\mathcal{I}$ the unit tensor.

The foil center of mass heaving motion $Z(t)$, and pitching motion $\theta(t)$ (see Fig. 1) are obtained through Newton's equations of motion.

$$m\ddot{Z} = b\dot{Z} + F_z, \tag{5}$$

$$J\ddot{\theta} = Ke + T_y, \tag{6}$$

where m is the foil mass and J its moment of inertial with respect to the rotation axis that points in the y direction that passes through the center of mass. The parameter b is the damping constant and the torque applied by the control is the term Ke, the error $e(t) = \theta_{ref} - \theta$ times the gain K. The control torque will try to rotate the foil to attain an angle of attack given by the reference angle $\theta_{ref}(t)$, and reduce the error e. The reference angle is changes to increase the lift F_z based on the behavior of a static NACA0015 foil. An angle θ_0 close but below the angle of maximum lift under static condition is chosen as the target for $\theta_{ref}(t)$. Since the foil is moving vertically with speed $\dot{Z}$, the estimate of the reference angle must include a correction due to the foil motion relative to the upstream flow [13], this is given by

$$\theta_{ref}(t) = \theta_0 + \arctan\left(\frac{\dot{Z}}{U}\right). \tag{7}$$

This dynamic reference angle will provide a feedback loop for the controller. In order to produce a heaving motion the control will change the sign of θ_{ref} whenever $Z(t)$ goes below $z = -h_0$ or beyond $z = h_0$. This produces a change in sign of the term Ke that makes the foil turn around and start moving in the opposite direction, which results in an oscillating heaving motion of an amplitude of about $2h_0$.

Scaling the problem with U, ρ and c, one finds a number of dimensional parameters that determine the solution. The main ones are

$$Re = \frac{\rho c U}{\mu}, \quad \Pi_1 = \frac{m}{\rho c^3}, \quad \Pi_2 = \frac{J}{\rho c^5}, \quad \Pi_3 = \frac{b}{\rho c^2 U},$$
$$\text{and} \quad \Pi_4 = \frac{K}{\rho U^2 c^3}.$$

These are the Reynolds number Re, two inertia numbers Π_1 and Π_2, a dimensionless damping coefficient Π_3 and a dimensionless control gain Π_4. Additionally, the parameter θ_0, and the length ratios s/c and h_0/c must be specified.

The resulting heaving motion of a certain frequency f can be used to compute a Strouhal number $St = fc/U$. Additionally, the cycle average power P extracted by the damper or wasted by the control torque, is used to compute the efficiencies $\eta = 2P/(\rho U^3 h_0 s)$.

3. The numerical schemes

For the two dimensional simulations (2D) the open source CFD software OpenFOAM was used [14]. It solves non steady Navier-Stokes equation through a second order Finite Volume Method named PIMPLE [15]. It also includes modules for solid-body interactions, moving surface fitting meshes, and mesh refinement [16]. In order to implement the feedback control loop, some modifications had to be carried out into the original (open source) code.

The module SixDOF was used to couple the fluid flow with the foil through the computation of hydrodynamic forces and torques and the solution of Newton's equations (5) and (6) [17]. The method for mesh deformation uses a diffusion equation with a variable coefficient to determine the nodes motion while fitting the foil boundary at all times. The mesh is composed of several regions with different levels of refinement. The highest level of refinement is a small region surrounding the surface of the airfoil, as shown in Fig. 2. It is contained in a larger deformable mesh, that can deform continuously while complying with the solid body motion of the internal mesh. This deformable mesh is circular and is itself

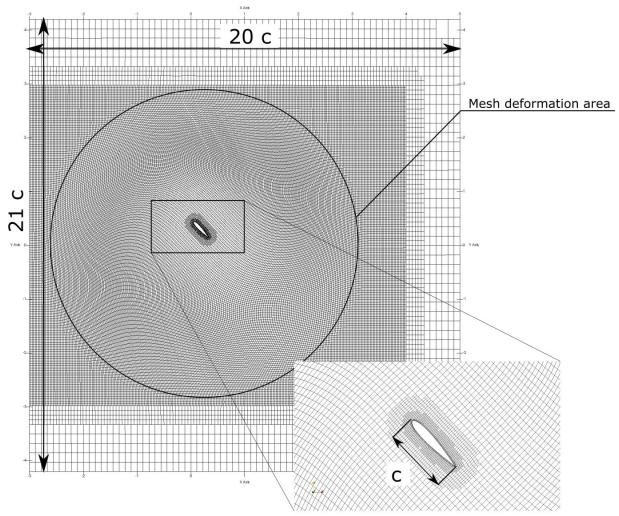

FIGURE 2. An example of a mesh used for two dimensional simulations with OpenFOAM. The mesh deformation region is shown, as well as a close view showing the finest mesh fitting the foil surface.

contained in a rectangular region called the refinement box, which lies inside the principal mesh, which follows with decreasing refinement until the domain boundaries are reached. The main disadvantage of this scheme is that large deformations of the mesh can cause numerical problems (largely deformed cells). This limits the final displacement of the airfoil. Additionally, the rotation of the body is limited to approximately 90 degrees. In spite of these limitations, this setup allowed for the simulation of the wingmill and the control scheme. Figure 2 shows the aforementioned regions and the dimensions of the mesh. Each mesh refinement step divides the mesh cell width and height by two. All the simulations had a minimum mesh width such as to fit at least four mesh cells inside the boundary layer near the airfoil surface.

Under idealized conditions, the boundary layer transition to turbulence for flows around thin airfoils occurs at Reynolds numbers in the range $5 \times 10^4 < Re < 2 \times 10^6$ [18]. Two dimensional simulation shown here correspond to non turbulent flows of $Re = 10^3$. Figure 3 shows snapshots of the vorticity behind the foil for 2D simulation of three different values of h_0.

For the three dimensional simulations (3D) a Lattice-Boltzmann Equation model for fifteen neighbors (known as a D3Q15 algorithm) was coded. The LBE method computes approximate solutions to the flow around the foil, Eqs. (1) and (2) for $\boldsymbol{u}$ and p. In LBE, the BGK approximation of the Boltzmann equation, from kinetic theory, is solved to obtain the distribution function in phase space of the fluid system [19]. Discretized statistical moments of the distribution functions are related to the $\boldsymbol{u}$ and p fields. Condition on the distribution function can be imposed to fulfill no-slip boundary conditions on $\boldsymbol{u}$ on curved boundaries [19]. These conditions can be extended to arbitrary surfaces [20]. Additionally, surface forces exerted on solid boundaries can be computed directly from the distribution functions [21], and used to compute forces and torques, Eqs. (3) and (4). To move the foil immersed in the square lattice, a Strömer-Verlet method is used to solve Eqs. (5) and (6). The present scheme is an extension to three dimensions of the algorithm used in [12]. This numerical scheme is explicit and very efficient when implemented to run in parallel architectures.

The flow domain is a rectangular region of lengths L_x, L_y and L_z. At $x = 0$ the velocity field is prescribed as $\boldsymbol{u} = U\hat{\boldsymbol{e}}_x$, while a zero velocity gradient condition is imposed at $x = L_x$ as well as at $y = 0, L_y$. Periodic boundary conditions are applied in the vertical boundaries $z = 0, L_z$. The wing center of mass is initially placed at $(L, L_y/2, L_z/2)$, and in horizontal position ($\theta = 0$). Starting form an initial $\boldsymbol{u} = U\hat{\boldsymbol{e}}_x$ everywhere and a uniform p field, the numerical simulation is run until a steady flow is obtained, before letting the foil perform pitching and heaving motions according to (3) and (4).

All 3D computations presented in this work correspond to $Re = 500$ and $L = 1.5c$, where the length of the chord c is of 100 lattice nodes. The computational domain size varies from $L_x = 4.8c$ to $6c$, $L_y = 1.6c$ to $3.2c$, and $L_z = 2.8c$ to $3.2c$. This corresponds to lattices with a number of nodes of the order of 10^7. All computations where performed on a

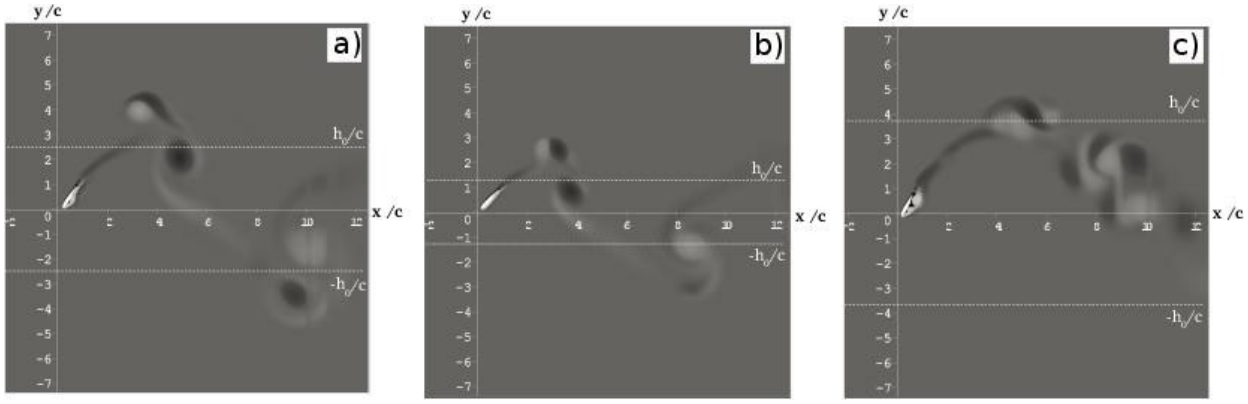

FIGURE 3. Vorticity fields. a)$\frac{h_0}{c} = 2.5$ and $B = 0.4$. b)$\frac{h_0}{c} = 1.25$ and $B = 0.4$. c)$\frac{h_0}{c} = 3.75$ and $B = 0.2$.

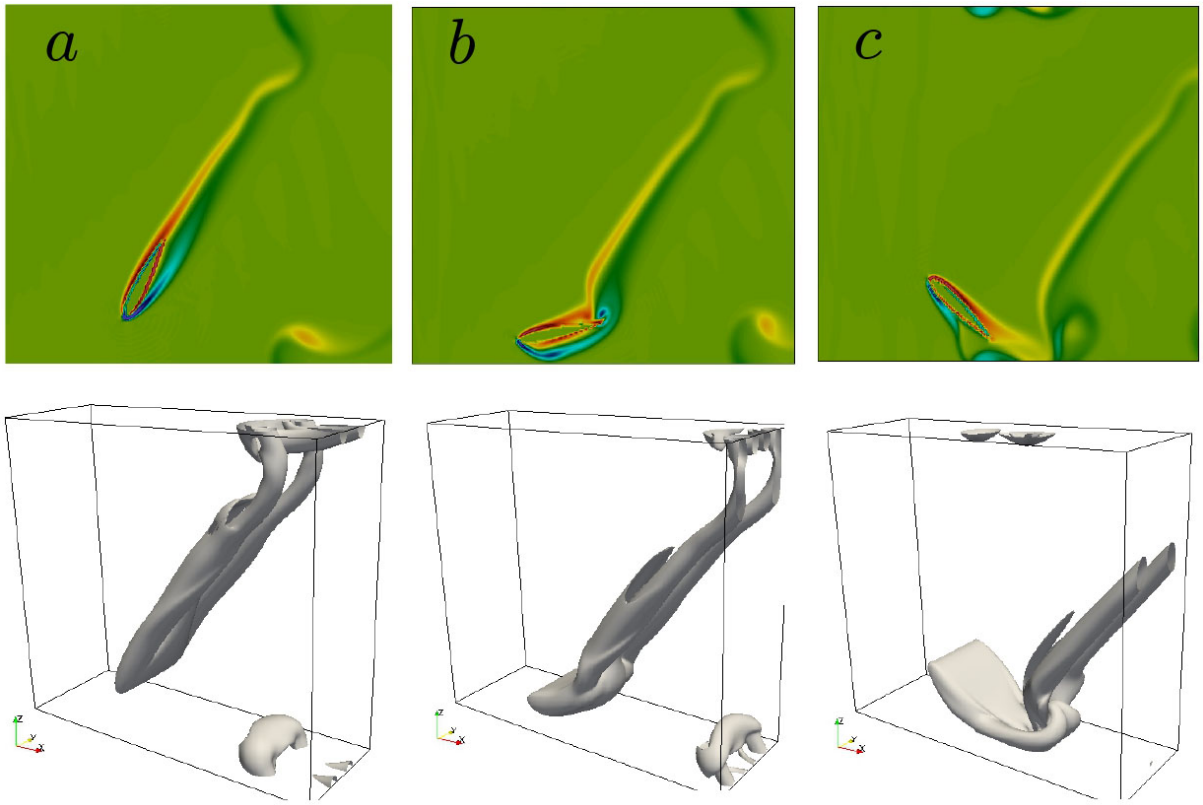

FIGURE 4. Vorticity of the flow around the 3D wingmill for $B = 0.857$, $h_0 = 1.5c$ and $s = c$. The y component at the top row and a surface of constant vorticity magnitude at the bottom row. Columns correspond to a sequence of times around the change of direction imposed by the control when $Z = L_z/2 - h_0$.

Nvidia Tesla K40 GPU, and typically took a couple of days to perform 10^5 time steps, corresponding to a number of heaving oscillations between 5 and 10. Figure 4 shows an example of the 3D simulations. At the top, the out of the plane component of vorticity is shown for a sequence of three times, and at the bottom a surface of constant vorticity is shown for the respective times. The implemented periodic boundary conditions can be observed in the figure.

4. Results

The instantaneous power extracted by the damper is $b\dot{Z}^2$. As the parameter Π_3 is increased so does b, but the generator (the damper) becomes stiffer and the average magnitude of the heaving speed $\dot{Z}$ decreases. Therefore the power extracted will show a maximum at some value of Π_3. Additionally, the power wasted by the control to adjust the angle of attack (to increase lift and consequently increase the magnitude of $\dot{Z}$) and to flip the foil is $Ke\dot{\theta}$. Hence, Π_4 will have an impact on the overall efficiency similar to that of Π_3. In view of preliminary results we chose to present results in terms of a parameter $B = \Pi_3/\Pi_4 = bUc/K$, that combines both effects.

Figure 5 shows the observed heaving motion, power and angles for the 2D simulations corresponding to $h_0/c = 2.5$ and $B = 0.375$. Presented at the bottom panel is the heaving motion Z (in arbitrary units) during a couple of oscillations along time (in arbitrary units). At the top, the evolution in radians of the reference angle (7) (dashed line) and the angle of attack $\theta(t)$ (continuous line) during these oscillations is shown. Notice that θ_{ref} changes sing just before the foil reaches its maximum (minimum) height, in order to make the

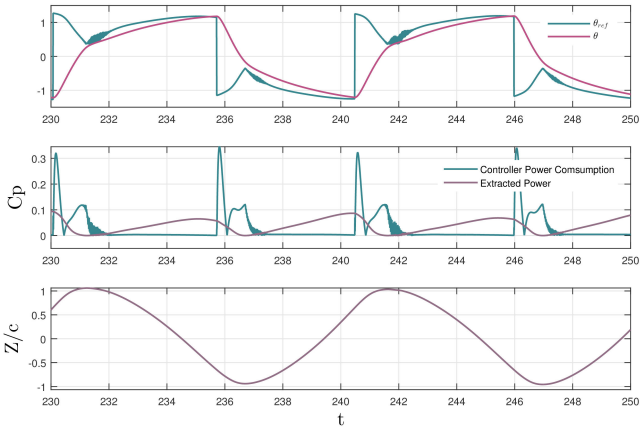

FIGURE 5. 2D simulations for $h_0/c = 2.5$ and $B = 0.375$. The vertical position of the foil vs time is shown at the bottom. At the middle, the power of the control and the damper are shown. At the top, θ and θ_{ref} are shown.

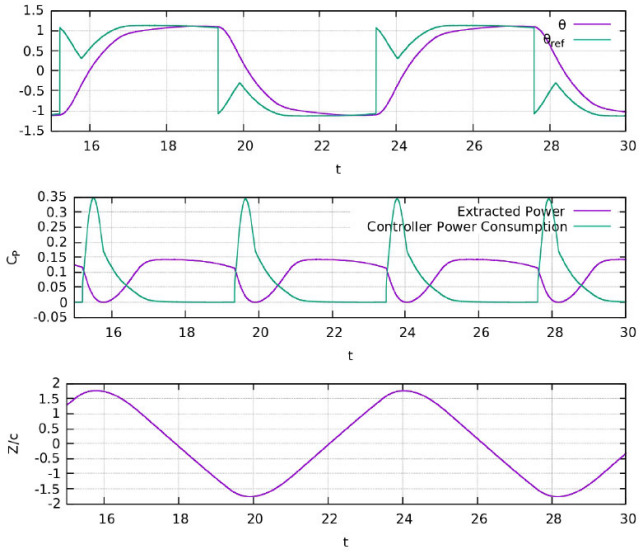

FIGURE 6. 3D simulations for $h_0/c = 1.5$ and $B = 0.857$ and $s = c$. The vertical position of the foil vs time is shown at the bottom. At the middle, the power of the control and the damper are shown. At the top, θ and θ_{ref} are shown.

control torque flip the foil and oscillate. In between these imposed changes of sign, θ_{ref} follows Eq. (7) reacting to the angle of attack $\theta(t)$, which is simultaneously driven by the control acting torque to follow θ_{ref} (Eq. (6)).

The graph at the middle of Fig. 5 shows the evolution in time, in arbitrary units, of the power consumed by the control torque and the power extracted by the damper. It can be seen that the control wastes a large amount of power when flipping the foil, but after that its contribution is negligible as θ gets close to θ_{ref}. As the angle of attack increases to reach θ_{ref}, lift increases and the foil moves faster, improving the power generated by the device. Notice that the net power (in this case the power of the damper) has a maximum in between the changes of sign of θ_{ref}. This observed behavior was either accompanied by detachment of the boundary layer and dynamic stall (see Fig. 3c)) or the result of the projection of the lift on the heaving direction z. Unlike the example presented in Fig. 5, heaving motion in the presence of dynamic stall is not uniform in between changes of sign of θ_{ref} and inflexion points appear.

Returning to the mentioned projection of the lift, the reference angle was chosen such as to have maximum static lift taking into account the changing motion relative to the upstream flow (see Eq. (7)). This change of reference causes this maximum lift to be projected onto the z axis (to obtain F_z), and so includes a factor of $\cos(\Delta\theta)$, where $\Delta\theta = \arctan(\dot{Z}/U)$. This causes the lift to decrease whenever the heaving speed becomes comparable to U. When this happens, the maximum of the power extracted coincides with that of $\cos(\Delta\theta)$. The correlation is clear when $\dot{y}/U \simeq 1$, as $\cos(\Delta\theta) \simeq 1 - (\dot{Z}/U)^2$ and the power extracted from the damping is proportional to $\dot{Z}^2$. An important consideration

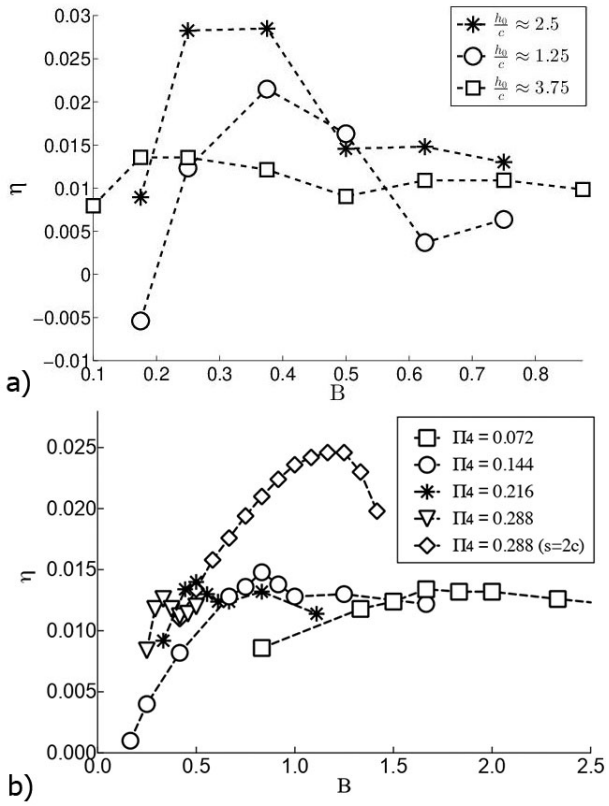

FIGURE 7. Efficiency η for different values of B. a) data for 2D simulations at $Re = 1000$ and for three values of h_0 are presented. b) Results for 3D simulations at $Re = 500$ are shown for a series of values of Π_4, $h_0 = 5c$ and $s = c$, except from the diamond plot where $s = 2c$.

since it limits the velocity and power that can be extracted using oscillating foils whose motion is constrained to a single axis.

Similar to Fig. 5, 6 shows the observed behavior of the 3D simulations for $h_0/c = 1.5$ and $B = 0.857$ and $s = c$. The graph in the bottom shows the vertical, heaving, position versus the dimensionless time for a couple of oscillations. Here as well, the wing moves uniformly in between turns during the heaving motion and does not shed vortices, only wing tip vortices appear (see Fig. 4a)). If the wing moves faster, boundary layer instabilities occur and vortices are shed. This can also happen if h increases, as instabilities need time to develop, or if we use a wider wing (an increase of s) as transverse instabilities appear (a 3D effect). Again, shedding a vortex produces small oscillation in the angle of attack θ and reduces lift and energy extraction. The graph on top in Fig. 6 shows the time evolution of θ and θ_{ref} similar to that shown in Fig. 5(top). Curves are less noisy than those observed in the 2D case, this is due to the more unstable flow simulated in 2D ($Re = 500$ in 3D). In the middle the power coefficient C_p, the power divided by $(1/2)\rho U^3 sc$, of the control action and the damper are shown to follow similar trends to those presented in 2D.

The device efficiency η for a set of parameter values con be found in Fig. 7, for both 2D and 3D simulations. The

graph at the top show the dependence of η on B for the 2D case and different values of h_0 and $Re = 1000$. Although not far from each other, the values of B where η is maximum for a given h_0 do not coincide. Additionally, as h_0 increases the maximum η appears to increase and then decay, presumably because for large values of h_0 there is more time for instabilities to develop and reduce efficiency. The graph at the bottom corresponds to the 3D case, $Re = 500$, $h_0 = 5$ and $s = c$ (except the data plotted with diamonds where $s = 2c$). The plots correspond to different values of Π_4 (the dimensionless gain K), so B changes through the change in the dimensionless damping coefficient Π_3. Results show that maximum efficiency for a given h_0 does not depend only on the parameter B. Results suggest also that foils with a larger wingspan are more efficient.

5. Conclusions

Fully coupled CFD-solid-body interaction schemes using a closed loop feedback control on an oscillating foil for current energy extraction (a wingmill device) were implemented to study flow and performance. OpenFOAM and a Lattice Boltzmann equation method were used for 2D and 3D simulations respectively. A proportional control law to follow a reference angle of attack based on the static airfoil characteristic curves was tested in order to attain maximum lift and improve performance. Foil kinematics was not imposed, and was driven by hydrodynamic forces and torques, and by the control torque, which represents an improvement with respect to previous studies.

Simulations show efficiencies lower than those observed in numerical studies with imposed kinematics (as expected). Results suggest that practical implementations should include passive mechanisms to switch the heaving direction of the foil and avoid the expensive control effort. Results also suggest that performance suffers when dynamic stall appears and whenever the heaving velocity $\dot{Z}$ is close to the upstream velocity U as the lift force (and power) starts to decrease due to the term $arctan(\dot{Z}/U)$ in equation (7).

The performance of the three dimensional finite-span wingmill follows similar trends to those observed in two dimensions. The variation of the net power cycle average on the parameter B (the dimensionless ratio between the damping coefficient and the control gain) has a maximum around the value of one for all numerical simulations performed so far. Scaling arguments to define B should be refined to explain the difference between the maximum values of the net power average.

Ground effects and the contribution from turbulence models are currently under study and will be reported elsewhere. We believe our scheme will allow the study of more elaborated control strategies and the search for optimal performance, which may help in the development of real wingmill devices.

The cases of foils with densities different from that of the surrounding fluid deserve to be studied. Variable foil densities can be easily included in our codes, and numerical studies will be performed in the near future. Based on studies of vortex induced vibrations (VIV) on cylindrical geometries without control schemes (see [22], for a review), we believe that the wingmill response to density variations can not be anticipated from the results in the present study. We expect complex fluid-structure interactions, of the sort observed in the VIV context. The observed critical mass for the appearance of large-amplitude vibrations, the existence of a "lock-in" region and the abnormal synchronization frequencies observed in the VIV context, suggest that the fluid-structure interaction within the wingmill device may share similar features.

Acknowledgements

B. Figueroa-Espinoza and D. Balam acknowledge the support of UNAM-DGAPA-PAPIIT grant No. IA102016. D. Balam thanks CONACYT for the support during his Ph.D. studies. C. Málaga acknowledges the support from UNAM-PASPA during his sabbatical stay at LIPC-UNAM. Special thanks to Gonzalo U. Martín Ruiz for his advise and support with hardware and software installation and maintenance. We gratefully acknowledge the support of NVIDIA Corporation with the donation of the Tesla K40 GPU used for this research.

1. W. Mkinney and J. DeLaurier, *J. Energy* **25** (1981) 109.
2. J. Young, J. C. Lai and M. F. Platzer, *Prog. Aerosp. Sci.* **67** (2014) 2.
3. Q. Zhu, *J. Fluid Mech.* **675** (2011) 495.
4. T. Kinsey and G. Dumas, *3rd Joint US-European Fluids Engineering Summer Meeting collocated with 8th International Conference on Nanochannels, Microchannels, and Minichannels*. (American Society of Mechanical Engineers 2010) 9.
5. A. Roberts, B. Thomas, P. Sewell, Z. Khan, S. Balman and J. Gillman, *J. Ocean Eng. Mar. Energy* **2** (2016) 227.
6. T. D. Finnigan, *Device for Capturing Energy from Fluid Flow.* (US 2010/0140933 A1).
7. Stingray Tidal Stream Energy Device - Phase 3. (The Engineering Business Ltd. Department of Trade and Industry Crown Copyright 2005).
8. Q. Xiao and Q. Zhu, *J. Fluid Struct.* **46** (2014) 174.
9. T. Kinsey and G. Dumas, *J. Fluids Eng.* **134** (2012) 071105.
10. Q. Zhu, *J. Fluid Struct.* **34** (2012) 157.
11. J. Wu, S. C. Yang, C. Shu, N. Zhao, and W. W. Yan, *J. Fluid Struct.* **54** (2015) 247.

12. F. Mandujano and C. Málaga, *Phys. Fluids* **30** (2018) 061901.
13. T. Kinsey and G. Dumas, *J. Fluids Eng.* **134** (2012) 031103.
14. G. J. Greenshields, *Programmers Guide*. (OpenFOAM Foundation Ltd. 2015).
15. J. H. Chow and E. Ng, *Int. J. Nav. Archit. Ocean Eng*. **8** (2016) 320.
16. R. O. Dwight, *Comput. Fluid Dynam.* (Springer 2006) 401.
17. E. Ekedah, 6-DOF VOF-solver without Damping in OpenFOAM. Project work for the Ph. D. course "*CFD with Open Source Software*". (Gothenburg, Sweden: Chalmers University of Technology 2008).
18. T. J. Mueller and J. D. DeLaurier, *Annu. Rev. Fluid Mech.* **35** (2003) 89.
19. Z. Guo, C. Zheng and B. Shi, *Phys. Fluids* **14** (2002) 2007.
20. A. D. Gallegos and C. Málaga, *Eur. J. Mech. B-Fluids*. **65** (2017) 464.
21. R. Mei, D. Yu, W. Shyy and L. Luo, *Phys. Rev. E* **65** (2002) 041203.
22. C. H. K. Williamson and R. Govardhan. *Annu. Rev. Fluid Mech*. **36** (2004) 413.